https://doi.org/10.5194/acp-2020-375
Preprint. Discussion started: 25 May 2020

Atmospheric Chemistry and Physics Discussions

The characterization of Taklamakan dust properties using a multi-wavelength Raman polarization lidar in Kashi, China

Qiaoyun Hu[1], Haofei Wang[2], Philippe Goloub[1], Zhengqiang Li[2], Igor Veselovskii[3], Thierry Podvin[1], Kaitao Li[2], and Mikhail Korensky[3]

[1]Univ. Lille, CNRS, UMR 8518 - LOA - Laboratoire d'Optique Atmosphérique, F-59000 Lille, France
[2]State Environmental Protection Key Laboratory of Satellite Remote Sensing, Aerospace Information Research Institute, Chinese Academy of Sciences, Beijing, China
[3]Physics Instrumentation Center of General Physics Institute, Troitsk, Moscow, 142190, Russia

Correspondence: Haofei Wang (wanghf@radi.ac.cn)

Abstract. The Taklamakan desert is an important dust source for the global atmospheric dust budget and a cause of the dust weather in Eastern Asia. The characterization of the properties and vertical distributions of Taklamakan dust in the source region is still very limited. To fill this gap, the DAO (Dust Aerosol Observation) was conducted in Kashi, China in 2019. Kashi site is about 150 km to the west rim of the Taklamakan desert and is strongly impacted by desert dust aerosols, especially in spring time, i.e. April and May. Apart from dust, fine particles coming from local anthropogenic emissions or/and transported aerosols are also a non-negligible aerosol component. In this study, we provide the first profiling of the $2\alpha + 3\beta + 3\delta$ lidar profiles of Taklamakan dust based on a multi-wavelength Raman polarization lidar. Four cases, including two Taklamakan dust events (Case 1 and 2) and two polluted dust events (Case 3 and 4) are presented. The lidar ratio in the Taklamakan dust outbreak is found to be 51±8 – 56±8 sr at 355 nm and 45±7 sr at 532 nm. The particle linear depolarization ratios are about 0.28±0.04–0.32±0.05 at 355 nm, 0.35±0.05 at 532 nm and 0.31±0.05 at 1064 nm. The observed polluted dust is commonly featured with reduced particle linear depolarization ratio and enhanced extinction and backscatter Ångström exponent. In Case 3, the lidar ratio of polluted dust is about 42±6 sr at 355 nm and 40±6 sr at 532 nm. The particles linear depolarization ratios decrease to about 0.25, with a weak spectral dependence. In Case 4, the variability of lidar ratio and particle linear depolarization ratio is higher than in Case 3, which reflects the complexity of the nature of mixed pollutant and the mixing state. The results provide the first reference for the characteristics of Taklamakan dust measured by Raman lidar. The data could contribute to complementing the dust model and improving the accuracy of climate modeling.

1 Introduction

Airborne dust is the most abundant aerosol species and accounts for nearly 35% of the total aerosol mass in the atmosphere (Boucher et al., 2013), with an annual flux of ∼2000 T yr^{-1} (Textor et al., 2006; Huneeus et al., 2011). According to the estimation of Ginoux et al. (2012), about 75% of the atmospheric dust is originated from natural emission and anthropogenic dust emission accounts for ∼25%. The area spreading from the Sahara desert, the Arabian Peninsula, Central Asia to East Asia is the most significant natural dust source. Based on model simulations, Tanaka and Chiba (2006) estimated that the Saharan

https://doi.org/10.5194/acp-2020-375
Preprint. Discussion started: 25 May 2020


Atmospheric Chemistry and Physics Discussions

desert contributes to ∼62% of the total dust emission and the contribution of Arabian Peninsula, Central Asia and East Asia is about half of the Saharan emission. The dust sources in North and South America, and Australia altogether account for about 25% of total emission. The suspending dust particles can directly influence the planetary radiation budget, and indirectly impact the climate through interfering with cloud properties and cloud process. Recent studies found that atmospheric dust is also linked to the activity of tropical cyclones and rainfall (Reed et al., 2019; Thompson et al., 2019).

A comprehensive dataset of dust properties is with significant importance for understanding the effects of dust in the ecosystem and for reducing the uncertainties of the climate model. However, this task is very challenging and needs the support of observation data. The properties of dust particles are determined by the texture of soils, the mineralogical compositions, vegetation cover and surface properties, which could vary globally from location to location. The modeling of dust horizontal and vertical distribution, and dust cycle, i.e. dust emission, transport and deposition, is crucial to the climatic modeling. This work demands also observational data as input and validation. So far, the vertically resolved information can only be obtained from lidar (Light detection and ranging). A multi-wavelength Raman polarization aerosol lidar can obtain multiple parameters at a vertical level. This capability makes it an useful tool for in aerosol study.

Compared with Saharan dust, the characterization of Asian dust is not adequately explored. In Asia, dust sources distribute over a large area and cover different terrain types. The high-elevated bare lands in Iran, Afghanistan and Tajikistan, and the Taklamakan desert in the Tarim basin, the Loess plateau and the Gobi desert in China are the main dust sources. In addition, excessive land-use and human activities could also form new dust source. There are a good number of publications reporting transported Asian dust observed in the downwind countries in East Asian (Liu et al., 2002; Murayama et al., 2004; Huang et al., 2008; Iwasaka et al., 2008). Long-range transported dust can cross the Pacific ocean and occasionally reach America (VanCuren and Cahill, 2002; Uno et al., 2009). However, very few field campaigns have been carried out for Asian dust study. The earliest field campaign characterizing Asian dust date back to 1989, when an experiment was carried out in Tajikistan for studying desert dust properties and the impact on meteorological conditions. The CADEX (Central Asian Dust EXperiment) project was planned to provide a data set of optical and microphysical properties of dust from Central Asia. Within this framework, a multi-wavelength Raman polarization lidar was deployed in Dushanbe, Tajikistan. This results in Hofer et al. (2017) provided important dust parameters, such as vertically resolved lidar ratios, linear depolarization ratios and mass concentrations. In 2002 and 2009, a elastic polarization lidar system (without Raman channel) was set up in Aksu (40.62°N, 80.83°E, in Xinjiang, China) near the north rim of Taklamakan desert (Kai et al., 2008; Jin et al., 2010). Jin et al. (2010) obtained the first lidar ratio of the Taklamakan dust in the source region, however, it requires extra assumptions and supplementary measurements. Sparse lidar observations in the downwind of transported Taklamakan dust have been reported but none of them provides intensive dust characteristics and the observation sites are far from the desert. Hence, a novel and comprehensive data set for the characteristics and vertical distribution of Taklamakan dust is important.

In 2019, the DAO (Dust Aerosol Observation) campaign was conducted in April to June in China. The first observation site in the DAO campaign is in Kashi (also called Kashgar) in April 2019, which is about 150 km to the western rim of the Taklamakan desert. The objective of the first session of DAO campaign is to study the characteristics of Taklamakan dust. The second session of the campaign was in Beijing in May and June, for investigating the impact of transported dust on the air

https://doi.org/10.5194/acp-2020-375
Preprint. Discussion started: 25 May 2020


Atmospheric Chemistry and Physics Discussions

quality in megacity. The main topic of this paper is the characterization of Taklamakan dust, therefore, only the measurements in Kashi will be presented. This study is organized into 5 sections. The description of DAO campaign is presented in Section 2, and the results and case study is in Section 3. The discussions and conclusions are presented in Section 4 and 5, respectively.

2 The DAO (Dust Aerosol Observation) campaign

2.1 Overview

The Taklamakan desert is located in the central of the Tarim Basin in the Uygur Autonomous Region of Xinjiang, China, covering an area of about 320,000 km^2. The mean elevation of the Taklamakan desert is about 1200–1500 m a.s.l (Petrov and S.Alitto, 2019). It is surrounded in three directions by high mountain ranges (see Figure 1). The observation site (39.51°N, 75.93°E, time zone: GMT+08:00) is in the northwest of the Kashi city and close to the border to Tajikistan, Kyrgyzstan and Afghanistan. Kashi features a desert climate with a big temperature difference between winter and summer. The coldest month is January with average temperature of -10.2–0.3°C and the warmest month is in July with average temperature of 18.6–32.1°C. The annual rainfall in Kashi is about 64 mm. The spring in Kashi is long and comes quickly. The rapidly heated surface sand in the desert could generate ascending currents which result in the frequent dust storm in springtime. This is the main reason that the field campaign was performed in springtime.

Except for desert dust, anthropogenic emission is the other important aerosol source. There are about 4.65 million habitants (predicted for 2017, see the link) in the Kashi prefecture, including the Kashi city and 11 subordinate counties. Kashi prefecture is a very populated region in Xinjiang with more than 1000 persons per square kilometer in the city center (Doxsey-Whitfield et al., 2015). Moreover, there are populated cities in the neighboring countries such as Kyrgyzstan, Tajikistan and Pakistan. Under favorable meteorological conditions, various aerosol, for example, pollution, could be potentially transported to Kashi and mix with dust aerosols.

2.2 Instrumentation and methodology

Lidar system

The multi-wavelength Raman polarization lidar is the main instrument installed in observation site. The lidar system, LILAS (Lille Lidar Atmosphere Study) has been operated in LOA (Laboratoire d'Optique Atmosphérique, Lille, France) since 2013 (Bovchaliuk et al., 2016; Veselovskii et al., 2016; Hu et al., 2019). During the DAO campaign, LILAS was transported from Lille to Kashi (and Beijing in the second session of the campaign) to perform observations. LILAS uses a Nd: YAG laser that emits at three wavelengths: 355, 532 and 1064 nm. The laser repetition rate is 20 Hz. A Glan prism is used to clean the polarization of the laser beam. The emitting power after the Glan prism is about 70, 90 and 100 mJ at 355, 532 and 1064 nm, respectively. LILAS system has three Raman channels, including 387 (vibrational-rotational), 530 (rotational) and 408 nm (water vapor). The backscattered light is collected using a 400 mm Newton telescope. The incomplete overlap range of LILAS system is about 1000–1500 m in distance, depending on the selected field of view angle. In the receiving optics, the three elastic

https://doi.org/10.5194/acp-2020-375
Preprint. Discussion started: 25 May 2020


Atmospheric Chemistry and Physics Discussions

channels are equipped with both a perpendicular and a parallel channel in order to measure the linear depolarization ratio at three wavelengths. The polarization calibration is performed following the $\pm 45^{\circ}$ method (Freudenthaler et al., 2009). During the DAO campaign, the polarization calibration has been performed at least once per day. LILAS can provide the profiles of the 2α+3β+3δ (2 extinction coefficients + 3 backscatter coefficients + 3 particle linear depolarization ratios) parameters. The Ångström exponent of the extinction coefficient and backscatter coefficient are calculated by the Equation 1:

$$\mathring{A} = -\frac{\log p(\lambda_1) - \log p(\lambda_2)}{\log \lambda_1 - \log \lambda_2} \tag{1}$$

where $p(\lambda)$ represents the optical parameters, such as AOD, extinction or backscatter coefficient at wavelength λ, $\mathring{A}$ represents the Ångström exponent of the corresponding parameters $p(\lambda)$. The statistical error of lidar derived parameters is estimated to be 10% for the extinction and backscatter coefficient, and 15% for the lidar ratios and particle linear depolarization ratios. The errors for the water vapor mixing ratio and relative humidity are about 20%. The other error sources, such as alignment of laser beam and errors in the selection of reference, are not considered in the error estimate.

Sun/sky photometer

Three sun/sky photometers are deployed in the Kashi observation site. One is affiliated to the AERONET (AErosol RObotic NETwork, Holben et al. (1998)) network and the other two are affiliated to SONET (Sun-Sky Radiometer Observation Network). SONET is a ground-based sun/photometer network with the extension of multi-wavelength polarization measurement capability to provide long-term columnar atmospheric aerosol properties over China (Li et al., 2018). The three sun/sky photometers provide complementary measurements by following different measurement protocols. In all, they can measure daytime aerosol optical depth (denoted as AOD hereafter) at 340, 380, 440, 675, 870, 1020 and 1640 nm, polarized/unpolarized sky radiances at 440, 675, 870 and 1020 nm and moon AOD as well. The succeeding data treatment and retrieval are performed following the protocols and standards of AERONET or SONET, depending on the affiliation of the instruments.

Satellite data

Satellite data have complementary advantages due to their large spatial coverage compared to ground-based remote sensing technique. In order to show the activity of the desert, we use the UV aerosol index (UVAI hereafter) derived from the OMPS (Ozone Mapping Profiler Suite) onboard the Suomi-NPP (National Polar-orbiting Partnership) satellite (Flynn et al., 2004; Seftor et al., 2014). OMPS provides full daily coverage data and the overpass time for Kashi region is around 06:30 UTC. The UVAI is calculated using the signal in the 340 and 380 nm channels (Hsu et al., 1999):

$$\text{UVAI} = -100 \times \left\{ \log_{10}\left[\frac{I_{340}}{I_{380}}\right]_{meas} - \log_{10}\left[\frac{I_{340}}{I_{380}}\right]_{calc} \right\}, \tag{2}$$

where $I_{...}$ represents the backscattered radiance at corresponding wavelength. The subscripts "meas" and "calc" respectively represent the real measurements and model simulation in a pure Rayleigh atmosphere. By the definition of UVAI, its positive values correspond to UV-absorptive aerosols such as desert dust and carbonaceous aerosols. Hence, the UVAI from OMPS is a good parameter for monitoring the activity of the Taklamakan desert.

https://doi.org/10.5194/acp-2020-375
Preprint. Discussion started: 25 May 2020


Atmospheric Chemistry and Physics Discussions

120 **Auxiliary data**

A radiosonde station (39.47°N, 75.99°N) in Kashi is 6 km to the observation site. The data are accessible on the website of the Wyoming weather data website (see the link). The radio sounding data are recorded at 00:00 and 12:00 every day at local time. They provide the vertical temperature and pressure profiles for the calculation of molecule scattering parameters in lidar data processing. The HYSPLIT (Hybrid Single-Particle Lagrangian Integrated Trajectory, Stein et al. (2015); Rolph et al. (2017))
125 model developed by the National Oceanic and Atmospheric Administration (NOAA) Air Resources Laboratory is used for the back trajectory of the air mass and for the air mass clustering. The HYSPLIT model is driven by the 0.5° gridded GDAS (Global Data Assimilation System) data and could produce the transport pathways of the air mass at different vertical levels. Besides, instruments measuring particulate matter (PM10 and PM2.5), gas concentration (SO2, O3 and NOx), particle size distribution, particle scattering and absorption coefficients, solar radiation and a cloud monitor are also deployed in the field
130 campaign. These data contribute to relevant air quality and solar radiation studies within the frame of the DAO campaign.

3 Results and analysis

3.1 Overview

Figure 2 presents the monthly averaged AOD at 500 nm, Ångström exponent between 440 and 870 nm and the FMF (fine mode fraction, the fraction of fine mode AOD to total AOD) in Kashi site from 2013 to 2017. The data are derived from
135 SONET network. The highest AOD occurs in spring, i.e. March and April, while the lowest values occur in summer time, i.e. June and July. The Ångström exponent is positively correlated to the FMF and negatively correlated to the AOD. The lowest mean Ångstöm exponent occurs in March and April, indicating that dust particles are dominant due to the seasonal increase of dust activities in this period (Littmann, 1991; Qian et al., 2002). In December and January, the Ångström exponent and FMF increase significantly, which proves that fine particles are an important aerosol source in Kashi. The fine particles are mostly
140 originated from heating, biomass burning, traffic and industrial pollution in the local area.

Figure 3(a) plots the AOD at 500 nm and the Ångström exponent measured during the DAO campaign in April 2019. The AOD varies from 0.07 to 4.70 and the Ångström exponent varies from 0.0 to 0.8. For AOD greater than 0.2, there is a high possibility that the corresponding Ångström exponent falls into the range of 0.0 to 0.2. While for AOD lower than 0.2, the Ångström exponent is mostly between 0.3 to 0.7. The negative correlation between the AOD and the Ångström exponent indicates that
145 coarse particles are the main cause for the increase of AOD. This argument is supported by the variation of the particulate matter plotted in Figure 3(b).

We select four representative cases from the nearly 1 month lidar observations. The four cases are recorded on 03, 09, 15 and 24 April 2019. The maps of UVAI are plotted in Figure 4. On 09 and 24 April, intense aerosol plumes were observed over the Taklamakan desert. One extreme dust event occurred on 24 April when the AOD (at 500 nm) reached about 4.70 at 08:40
150 UTC, with instantaneous Ångström exponent about -0.02 and the visibility about 1 km. The PM10 increased to the monthly maximum on 24 April, reaching nearly 1500 $\mu g/m^3$. High aerosol content makes the cloud screening difficult, so the accuracy of the measured AOD might degrade due to uncertain cloud contamination. On 03 and 15 April, the activity of the Taklamakan

https://doi.org/10.5194/acp-2020-375
Preprint. Discussion started: 25 May 2020


Atmospheric Chemistry and Physics Discussions

desert became less intense compared to the first two cases. The concentration of dust particles decrease and the features of polluted dust appear. Lidar quicklooks at 532 nm for the four cases are plotted in Figure 5.

3.2 Case studies

3.2.1 Case 1: 09 April 2019

Dust plumes over the Taklamakan desert are detected on 07, 08 and 09 April, shown in Figure 4. The most intense plume in the three days appeared on 07 April, with maximum UVAI about 4.0. On 09 April, a belt-like plume appeared in the north and northwest of the desert. Figure 5(b) shows the range-corrected lidar signal at 532 nm collected between 9 and 10 April. The boundary layer height slightly increases from 3000 m to 4000 m in the night, and strong backscattered lidar signal is seen below 2000 m. Figure 6 shows the profiles of the optical properties, water vapor mixing ratio (WVMR) and relative humidity (RH) averaged between 17:00 and 22:00 UTC, 09 April 2019. The extinction coefficients generally decrease with height. At 1000 m, the extinction coefficients are greater than 0.5 km^{-1} and remain almost stable below 2000 m. The RH is no more than 40$\pm$8% below 2000 m and rises to 60$\pm$12% at 3800 m. The lidar ratio varies between 40$\pm$6 and 48$\pm$7 sr at 532 nm and between 55$\pm$8 and 62$\pm$9 sr at 355 nm. The particle linear depolarization ratio (PLDR) is about 0.32$\pm$0.05 at 355 nm and 0.36$\pm$0.05 at 532 nm. The volume linear depolarization ratio (VLDR) at 1064 nm is about 0.32$\pm$0.03. The backscatter coefficient, as well as the PLDR at 1064 nm is not available above 1800 m, due to the distortion of 1064 nm lidar signal caused by the high concentration of dust particles. We can expect that the VLDR is approximate to PLDR at 1064 nm under this condition, since the dust content is so high that molecular scattering at 1064 nm can be neglected. The $EAE_{355-532}$ is about -0.10$\pm$0.30 at 800 m and rises to 0.10$\pm$0.30 at 3800 m. The Ångström exponent of backscatter coefficient ($BAE_{355-532}$) is negative and varies from -0.7$\pm$0.3 to -0.4$\pm$0.3. Below 3000 m, the lidar ratios mildly decrease with height, while the PLDRs do not show obvious vertical variations. Above 3000 m, the vertical variations in the lidar ratios and PLDRs become more significant. The vertical variations of the lidar ratios and PLDRs are possibly the result of particle sedimentation or/and vertically dependent particle origins.

On 09 April, the Taklamakan desert is covered by a low-pressure zone with easterly and northeasterly wind prevailing over the western part of the desert. It is a favorable condition for the elevation of dust particles. Figure 7 shows the 48-hour back trajectory ending at 20:00 UTC for air mass at 1000, 2000 and 3000 m. The air masses at the three vertical levels are originated from the Taklamakan desert. They all passed over the area where dust plumes have been observed and then diverged when approaching the rim of the desert. In the end, the air masses at 1000, 2000 and 3000 m arrived at the observation site from the northeast, east and southeast respectively, after being lifted from near the surface.

3.2.2 Case 2: 24 April 2019

On 24 April, the observation site was enclosed by floating dust. In the daytime, the sky radiance dropped below the detection limit of the sun/sky photometer, so the AERONET and SONET retrieval can not be applied. A large and intense plume was

https://doi.org/10.5194/acp-2020-375
Preprint. Discussion started: 25 May 2020


Atmospheric Chemistry and Physics Discussions

first detected in the morning of 23 April 2019 (Figure 4). And on 24 April, a hot spot of UVAI appeared over the observation site. The daily average of AOD is 3.63 and Ångström exponent is about -0.01, according to the daytime sun/sky photometer measurements. The lidar quicklook on 24 April in Figure 5 shows that the boundary layer height rises from about 1200 m to 2000 m from 14:00 to 24:00 UTC. Due to the high dust attenuation in the boundary layer, both sun/sky photometer and lidar cannot detect whether clouds exist on 24 April. Figure 8 plots the averaged parameters between 15:00–24:00 UTC, 24 April 2019. The dust layer was so thick that the laser beam can not penetrate. The amplitude of Raman signal dropped by 5–6 orders in the lower 2000 m. In this condition, we can not find a aerosol-free zone to for the calibration of lidar signal, therefore, the calculation of the backscatter coefficient using Raman method is not possible. But the extinction coefficient can be derived from the Raman signal (Ansmann et al., 1992). The extinction coefficients are 1.0 ± 0.1 km^{-1} at 800 m and increases to about 1.5 ± 0.2 km $^{-1}$ at 1500 m. The extinction coefficient at 355 nm is removed at above 1500 m because it starts to oscillate due to insufficient signal-to-noise ratio. The extinction coefficient at 532 nm decreases to about 1.1 ± 0.1 km^{-1} at 2000 m. By assuming that the lidar ratios are about 55 sr and 45 sr at 355 and 532 nm, respectively, we obtain the backscatter coefficient from the extinction coefficient, and then calculate the PLDRs (in Figure 8(c)). The PLDR is about 0.32 at 355 nm and 0.37 at 532 nm, which are rather consistent with the results in Case 1. The uncertainties of the PLDRs are not accessible because the uncertainties of the assumption of lidar ratio are not known.

The back trajectories (not shown) indicates that dust particles (at 1000 and 2000 m) are originated from the northeast and east, where intense dust plumes were observed on 23 and 24 April. Figure 9 shows synoptic conditions at 00:00 UTC, 23 April and 06:00 UTC, 24 April. The meteorological conditions on 23 and 24 April are favorable for dust emission, similar to Case 1. The Taklamakan desert is enclosed by a low-pressure zone (Figs. 9(a) and (c)). The plume observed by OMPS on 23 April was probably lofted in the local morning. In the eastern part of the Taklamakan desert, 37–39°N, 83–88°E, the wind velocity at 10 m (a.g.l) reaches more than 50 km/h (Figure. 9(a)) and at 850 hPa level the maximum wind velocity reaches 90 km/h (Figure. 9(b)). The high wind velocity near the surface and large vertical wind gradient help elevate dust particles from the surface into the atmosphere. On 23 and 24 April, easterly and northeasterly wind are prevailing in the desert region, thus blowing the lifted dust particles to the observation site.

3.2.3 Case 3: 15 April 2019

The daily mean AOD on 15 April was 0.63, and the Ångström exponent was about 0.10. Compared to the previous two cases, the Ångström exponent increase obviously. The boundary layer height started to increase at 15:00 UTC and stayed at 3500 m in the night of 15 April. Cirrus clouds were continuously present during the period of lidar measurement (Figure 5(c)). The lidar derived parameters between 18:00–20:00 UTC are plotted in Figure 10. The extinction coefficients in the boundary layer are about 0.15 km^{-1} and decrease to almost zero at 3500 m. The RH increases up to $60\pm12\%$ at 2200 m. Below this height, the lidar ratio, PLDR, EAE and BAE are almost stable. The lidar ratio is about 51 ± 8 sr at 355 nm and 45 ± 7 sr at 532 nm. The PLDRs at 355, 532 and 1064 nm are around 0.32 ± 0.05, 0.34 ± 0.05 and 0.31 ± 0.05, respectively. The $EAE_{355-532}$ is about 0.02 ± 0.30, showing a gentle increase with height, and the $BAE_{355-532}$ is about -0.29 ± 0.30. Above 2200 m, the RH starts to increase and reaches its maximum, i.e. $80\pm16\%$, at 2800 m. The $EAE_{355-532}$ and $BAE_{355-532}$ increase to 0.10 ± 0.30 and

https://doi.org/10.5194/acp-2020-375
Preprint. Discussion started: 25 May 2020


Atmospheric Chemistry and Physics Discussions

-0.06±0.30, respectively. On contrary, the lidar ratios and PLDRs decrease and reach the minimum at about 2800 m. The lidar ratio is about 40±6 sr at 2400–2800 m, with a weak spectral dependence, and the PLDRs are about 0.23±0.03 at 355 nm, 0.26±0.04 at 532 nm and 0.24±0.03 at 1064 nm. It should be noticed that the backscatter coefficient at 1064 nm is performed using Klett method with an assumption of lidar ratio equal to 40 sr (Klett, 1985).

Dust activities were observed by the OMPS on 13 and 15 April 2019 (Figure 4), while the intensity was less stronger than in Case 1 and 2 and the distance between the dust plume and the observation site is farther. The 48-hour back trajectories ending at 19:00 UTC are shown in Figure 11. Air masses at the three vertical levels (1000, 2000 and 3000 m) are originated from the eastern part of the Taklamakan desert, where no intense dust activities have been observed by OMPS in the recent three days. It explains the decrease of dust content in the boundary layer. When dust loading decreases, the impact of fine mode particles emerges. The changes of EAE, BAE, PLDR and lidar ratios above 2200 m is a clear evidence of polluted dust. The pollution could be lifted up from the ground in local area by convection or be transported from other area. Additionally, the RH at above 2500 m is about 60±12%–80±16%, which could lead to the hygroscopic growth of some aerosol species. Pure dust is regarded as hydrophobic aerosols because its compounds are insoluble, but when coated by hygroscopic aerosol species, for example, nitrate, the polluted dust could become hygroscopic. The fine mode particles can be hydrophobic or hydroscopic, depending on their chemical compositions(Carrico et al., 2003; Shi et al., 2008; Pan et al., 2009). In this case, the occurrence of hygroscopic growth is not evident.

3.2.4 Case 4: 03 April 2019

The daily mean AOD on 03 April is 0.16 and the Ångström exponent is about 0.11. The boundary layer height is about 3000 to 4000 m, rising slightly in the night of 03–04 April. Starting from 16:30 UTC, some liquid cloud layers occurred at the top of the boundary layer (Figure 5(a)). Figure 12 shows the profiles derived from lidar observations at 14:00–16:00 UTC, 03 April. The extinction coefficients decrease from about 0.28±0.03 km^{-1} at 1000 m to about 0.10±0.01 km^{-1} at 3000 m, with $EAE_{355-532}$ ($BAE_{355-532}$) increasing from 0.01±0.30 (-0.38±0.3) to 0.28±0.30 (0.02±0.30). Below 2100 m, the lidar ratios are about 45±7 sr at 532 nm and 51±8 sr at 355 nm. The PLDRs are about 0.35±0.05 at 532 nm and 0.32±0.05 at 1064 nm and 0.28±0.04–0.32±0.05 at 355 nm. Between 2100 and 3000 m, the variation of lidar ratios is not monotonic. At 2500 m, the lidar ratios reach the minimum of 38 ± 6 sr at 532 nm and 42 ± 6 sr at 355 nm. The lidar ratios, $BAE_{355-532}$ and $EAE_{355-532}$ at this height all coincide well with the values at the boundary layer top in Case 3, which suggests the presence of polluted dust particles in Case 4. Above 2500 m, the lidar ratios and the RH (also the WVMR) re-increase, with the PLDRs decreasing. These signs may suggest the existence of a different aerosol types between 2500 and 3000 m.

Figure 13 plots the 72-hour back trajectories for 1000, 2000 and 3000 m. Air masses at 1000 and 2000 m are from the Taklamakan desert, while the air mass at 3000 m is from Central Asia. When extending the trajectory duration to 96 hours, the results (not plotted) suggest that air mass at 3000 m is originated from North Africa. This finding suggests that dust particles observed in Kashi may have a proportion of long-transported aerosol component. The air mass clustering based on 24-hour back trajectories indicates that about 52% of air mass at 3000 m is from North Africa and Arabian Peninsula. At 3500 m, this proportion increases to 74% and there is also a fraction of air mass coming from Europe. In the long transport pathway, aerosol

https://doi.org/10.5194/acp-2020-375
Preprint. Discussion started: 25 May 2020


Atmospheric Chemistry and Physics Discussions

properties could modify due to deposition and mixing with various aerosols. Hence, the complexity of aerosol properties at the boundary layer top is difficult to be resolved.

4 Discussion

The optical parameters in the 4 cases are summarized in Table 2. In order to distinguish Taklamakan dust observations, we define Taklamakan dust by $EAE_{355-532}$ smaller than 0.1 and $PLDR_{532}$ greater than 0.32 at 532 nm. Back trajectories are also used as a reference for identifying the aerosol origins. The observations falling beyond this category are classified as polluted dust.

Aerosol source

The coarse-mode dust and fine-mode particles originated from anthropogenic emission or transport are the two important aerosol components in Kashi. During the campaign, dust is undoubtedly the predominant component. In the dust storms (Case 1 and Case 2), dust particles are lifted from the Taklamakan desert by the low-pressure system along with strong wind, and then blown to the observation site by the easterly or northeasterly wind. The influence of pollution is not clearly seen in the dust storms. However, when the activities of the Taklamakan desert wane and dust concentration becomes lower, the impact of pollution emerges. Observations in Case 3 and 4 clearly demonstrate the contrast of dust in the lower boundary layer and polluted dust particles at the boundary layer top. During the 1-month campaign, the traces of pollution, featured with increased $EAE_{355-532}$ and decreased PLDRs are frequently observed.

The evidence of pollution in Taklamakan dust has been found in previous in-situ measurements. Huang et al. (2010) sampled aerosol particles in springtime at Tazhong site, which is located in the north rim of Taklamakan desert, and found that the As element was moderately enriched. The As element is a tracer of pollution, originated probably from coal burning. It is also found that the concentration of sulfate in Taklamakan dust is at a high level. The increased concentration of sulfate in the Taklamakan dust could be related to the provenance of the Taklamakan desert, because it is speculated to be ocean 5–7 millions years ago (Sun and Liu, 2006). Sulfate could also come from anthropogenic emission, for example, the uptake of the SO2 gases. Iwasaka et al. (2003) examined the aerosol samples by the electron microscopy in Dunhuang, China, which is in the downwind of transported Taklamakan dust. They found that mineral dust is the main component in the coarse-mode aerosols, while in the fine mode, ammonia sulfate, which is mainly from anthropogenic emissions, is the major component. These studies indicate that the Taklamakan dust near the source region have been contaminated by other aerosol species with anthropogenic origins. It is in agreement with our conclusion, however, in this study we cannot clarify the exact involving aerosol species and the mixing state in the polluted dust. In our study, polluted dust mostly appeared at the boundary layer top, which agrees with the finding of Iwasaka et al. (2003). These fine particles are possibly lifted by convective air flow and concentrate at higher altitude as bigger particles settle down. The mixing of mineral dust with these aerosol species can modify their properties of light scattering, hygroscopic properties and interfere the cloud process (Kojima et al., 2006; Fan et al., 2016).

Long-range transported aerosols are another possible aerosol source in Kashi. Based on model simulations, some previous studies have reported intercontinental dust transport from North Africa or the Middle East to the East Asia (Park et al., 2005;

https://doi.org/10.5194/acp-2020-375
Preprint. Discussion started: 25 May 2020


Atmospheric Chemistry and Physics Discussions

Tanaka et al., 2005; Sugimoto et al., 2019). Figure 14 plots the air mass clustering for three different vertical levels in April 2019. The contribution of air masses from the west, such as Central Asia, Middle East, Europe and North Africa always exists and the influence increases with height. At 1000 m, the main aerosol source is from the Taklamakan region and accounts for only 73%. At 3000 m, air mass from Central Asia, Middle East and North Africa accounts for about 51%, and there is about 2% of air mass from Europe. While at 4000 m, air mass from the Taklamakan occupies only 29% and the rest are from Central Asia, the Middle East and North Africa. The west-to-east airmass transport are associated with the midlatitude westerlies, which is a continuous force for air mass transport (Yumimoto et al., 2009; Yu et al., 2019). There are various aerosol sources in the intercontinental transport pathway, such as Saharan dust from North Africa, Middle East and Central Asia, pollution and biomass burning from East Europe. And the aerosol properties could be modified during the transport. Hence, it is difficult to find out the exact aerosols brought to the site.

Lidar ratio and depolarization ratio

We found that, for Taklamakan dust, the lidar ratios are about 45±7 sr at 532 nm and 51–56±8 sr at 355 nm. The PLDRs are about 0.28–0.32±0.05 at 355 nm, 0.35±0.05 at 532 nm and 0.31±0.05 at 1064 nm. Polluted dust in Case 3 has lidar ratio of about 42±6 sr at 355 nm and 40±6 sr at 532 nm; and PLDR of about 0.23±0.03, 0.26±0.03 and 0.24±0.03 at 355, 532 and 1064 nm, respectively. In Case 4, the lidar ratio of polluted dust varies non-monotonically in the range of 43±6 to 57±8 sr at 355 nm and 38±6 to 49± 8 sr at 532 nm. The PLDRs vary in the range of 0.21±0.03–0.29±0.04 at 355 nm, 0.28±0.04–0.34±0.05 at 532 nm, and 0.28±0.04–0.33±0.05 at 1064 nm.

Table 3 presents an overview of the lidar ratios and PLDRs of Asian dust, Saharan dust and American dust in previous publications. Jin et al. (2010) derived a lidar ratio of 42±3 sr at 532 nm for Taklamakan dust, which agrees well with our results. The observation site in Jin et al. (2010) was very close to Kashi, however, their results were based on the observations of an elastic lidar, so it requires the assumption of vertically independent lidar ratio and complementary measurements. Hofer et al. (2017) reported lidar ratios (PLDRs) of 47±2 sr (0.23±0.01) at 355 nm and 43±3 sr(0.35±0.01) at 532 nm, based on Raman lidar observations in Dushanbe (Tajikistan) on 8 August 2015. Dieudonné et al. (2015) obtained similar results (at 355 nm) in Kazan and Omsk (Russia) for dust originated from the Caspian sea and the Aral sea. Murayama et al. (2004) observed transported Asian dust in Japan and derived lidar ratio about 49 sr at 355 and 43 sr at 532 nm. A special case is on 14 July 2016 in Hofer et al. (2017) when an extreme dust event was observed. The lidar ratios (PLDRs) were estimated to be 40±1 sr (0.29±0.01) at 355 nm and 39±1 sr (0.35±0.01) at 532 nm. The PLDRs are consistent with Taklamakan dust, but the lidar ratios at 355 and 532 nm are both lower than in our study. Moreover, the lidar ratios at 355 and 532 nm in this case are very close. While in our study the lidar ratio of Taklamakan dust at 355 nm always exceeds that at 532 nm.

In Saharan dust observations, both spectrally dependent and independent lidar ratios at 355 and 532 nm have been reported. Tesche et al. (2009) found 53–55 sr at 355 and 532 nm, based on the Raman lidar measurements in SAMUM campaign at Ouarzazate. Groß et al. (2011) found lidar ratios of 48–70 sr in Cape Verde using high spectral resolution lidar. In the SHADOW2 campaign, it is found that, in the dry season (November to March), the lidar ratio was 60±9–75±11 sr at 355 nm and 45±7–55±8 sr at 532 nm. While in the transition period from the dry to wet season, the lidar ratios were about 50±8–

https://doi.org/10.5194/acp-2020-375
Preprint. Discussion started: 25 May 2020


Atmospheric Chemistry and Physics Discussions

60±9 sr at both 355 and 532 nm. The seasonal change of lidar ratios reflects the variation of dust absorption, which is resulted from the seasonal change of wind direction (Hu, 2018; Veselovskii et al., 2016, 2020).

The comparison indicates that the lidar ratios of Asian dust are generally lower than Saharan dust, which might be explained by the difference of dust absorption. Biagio et al. (2019) presented that the SSA (single scattering albedo) of Taklamakan dust sample is greater than Sahel dust, after investigating 19 dust samples collected from global dust sources. Studies found that the absorption of dust is closely correlated to the content of iron oxides, whose content varies in different geographical dust source (Moosmüller et al., 2012; Biagio et al., 2019). Other factors, such as the particle size distribution, shape and so on, can also determine dust lidar ratio. Moreover, pollution could be another another that impact dust properties. In Asia, there are more potential anthropogenic pollution sources compared with in Africa. The Case 3 in this study shows that dust lidar ratios decrease when mixed with pollution. Depending on the state of mixing and the type of the mixed aerosols, the contamination of pollution could modify the properties of dust. The PLDRs of Asian dust, Saharan dust and American dust mostly fall in the range of 0.23–0.28 at 355 nm. While the PLDR at 355 nm for Taklamakan dust reaches as high as 0.31–0.32. The highest PLDRs at 532 and 1064 nm have been observed in American dust that appeared near its source region. The PLDR at 532 nm is the one measured the most often. Its values vary in the range of 0.30–0.35 when the observation site is close to the dust source. After long-range transport, the PLDR at 532 nm clearly decreases. Thus, we speculate that the high PLDR at 355 nm in Taklamakan dust might be linked to the distance of the observation site to the dust source. Shorter transport distance helps avoid the loss of big particles and the mixing of dust with other types of aerosols.

5 Conclusions

The first session of DAO campaign was conducted in Kashi, China in April 2019. The objective of DAO campaign is to provide a comprehensive characterization of Taklamakan dust using multi-wavelength lidar measurements. During the nearly 1 month campaign, we found that, dust particles, originated mainly from the Taklamakan desert, are the dominant aerosol component in springtime in Kashi, while the influence of fine-mode particles needs also to be considered. Kashi is a populated region, pollution emitted from anthropogenic activities very likely the main component in fine-mode aerosols. Additionally, air mass clustering using the HYSPLIT model suggests that long-range transported aerosols from Africa, Europe, the Middle East and Central Asia could be a potential aerosol source in Kashi. This study provides the first characterization of the spectral lidar ratio and PLDRs of the Taklamakan dust. The results fill the gap of the characterization of Taklamakan dust and provide reference for succeeding studies and for implementing the climate modeling. This study also points out the importance of considering the dust mixing with pollution in climate modeling. Our results show that, in the most dusty season of the year and in an observation site of 150 km to the desert, the observed Taklamakan dust has already been polluted. Pollution could alter the optical and microphysical properties of dust particles, thus influencing the direct radiative radiation. Moreover, polluted dust could modify the cloud formation process by acting as cloud condensation nuclei and ice nuclei, which will impose indirect

https://doi.org/10.5194/acp-2020-375
Preprint. Discussion started: 25 May 2020


Atmospheric Chemistry and Physics Discussions

influence on the earth's radiation budget and the long-term climate change. There is a collection of cases about the interactions of polluted dust and clouds in the DAO campaign and this study well be presented in the next step.

Data availability. The satellite data from OMPS and AIRS can be found in NASA's GES DIS service center. The meteorological data, GDAS data and the HYSPLIT dispersion model are available in the NOAA ARL site (https://ready.arl.noaa.gov/HYSPLIT.php). All the other data presented in this study are available upon any request of readers.

Author contributions. The project was supervised by PG and ZL. QH, TP and IV were in charge of the Lidar operation and maintenance. QH, IV and HW performed the data analysis. QH wrote the manuscript of this paper. KL provide the sun/sky photometer data. MK helped in the lidar operation and instrument preparation.

Competing interests. The authors declare that they have no conflict of interest.

Acknowledgements. We acknowledge the colleagues in the Institute of Remote Sensing and Digital Earth for their kind help and for the financial support. And we thank the colleagues in the GPI RAS (Prokhorov General Physics Institute of the Russian Academy of Sciences), LOA, ESA/IDEAL+ project and IAP (Institue of Atmospheric Physics) for the participation and the efforts they have made for the campaign.

https://doi.org/10.5194/acp-2020-375
Preprint. Discussion started: 25 May 2020


Atmospheric Chemistry and Physics Discussions

References

Ansmann, A., Riebesell, M., Wandinger, U., Weitkamp, C., Voss, E., Lahmann, W., and Michaelis, W.: Combined Raman elastic-backscatter lidar for vertical profiling of moisture, aerosol extinction, backscatter, and lidar ratio, Applied Physics B: Lasers and Optics, 55, 18–28, 1992.

Ansmann, A., Bösenberg, J., Chaikovsky, A., Comerón, A., Eckhardt, S., Eixmann, R., Freudenthaler, V., Ginoux, P., Komguem, L., Linné, H., et al.: Long-range transport of Saharan dust to northern Europe: The 11–16 October 2001 outbreak observed with EARLINET, Journal of Geophysical Research: Atmospheres, 108, 2003.

Biagio, C. D., Formenti, P., Balkanski, Y., Caponi, L., Cazaunau, M., Pangui, E., Journet, E., Nowak, S., Andreae, M. O., Kandler, K., et al.: Complex refractive indices and single-scattering albedo of global dust aerosols in the shortwave spectrum and relationship to size and iron content, Atmospheric Chemistry and Physics, 19, 15 503–15 531, 2019.

Boucher, O., Randall, D., Artaxo, P., Bretherton, C., Feingold, G., Forster, P., Kerminen, V.-M., Kondo, Y., Liao, H., Lohmann, U., et al.: Clouds and aerosols, in: Climate change 2013: the physical science basis. Contribution of Working Group I to the Fifth Assessment Report of the Intergovernmental Panel on Climate Change, pp. 571–657, Cambridge University Press, 2013.

Bovchaliuk, V., Goloub, P., Podvin, T., Veselovskii, I., Tanre, D., Chaikovsky, A., Dubovik, O., Mortier, A., Lopatin, A., Korenskiy, M., et al.: Comparison of aerosol properties retrieved using GARRLiC, LIRIC, and Raman algorithms applied to multi-wavelength lidar and sun/sky-photometer data, Atmospheric Measurement Techniques, 9, 3391–3405, 2016.

Burton, S., Hair, J., Kahnert, M., Ferrare, R., Hostetler, C., Cook, A., Harper, D., Berkoff, T., Seaman, S., Collins, J., et al.: Observations of the spectral dependence of linear particle depolarization ratio of aerosols using NASA Langley airborne High Spectral Resolution Lidar, Atmospheric Chemistry and Physics, 15, 13 453–13 473, 2015.

Carrico, C. M., Kus, P., Rood, M. J., Quinn, P. K., and Bates, T. S.: Mixtures of pollution, dust, sea salt, and volcanic aerosol during ACE-Asia: Radiative properties as a function of relative humidity, Journal of Geophysical Research: Atmospheres, 108, 2003.

Dieudonné, E., Chazette, P., Marnas, F., Totems, J., and Shang, X.: Lidar profiling of aerosol optical properties from Paris to Lake Baikal (Siberia), Atmospheric Chemistry and Physics, 15, 5007–5026, 2015.

Doxsey-Whitfield, E., MacManus, K., Adamo, S. B., Pistolesi, L., Squires, J., Borkovska, O., and Baptista, S. R.: Taking advantage of the improved availability of census data: a first look at the gridded population of the world, version 4, Papers in Applied Geography, 1, 226–234, 2015.

Esselborn, M., Wirth, M., Fix, A., Weinzierl, B., Rasp, K., Tesche, M., and Petzold, A.: Spatial distribution and optical properties of Saharan dust observed by airborne high spectral resolution lidar during SAMUM 2006, Tellus B: Chemical and Physical Meteorology, 61, 131–143, 2009.

Fan, J., Wang, Y., Rosenfeld, D., and Liu, X.: Review of aerosol–cloud interactions: Mechanisms, significance, and challenges, Journal of the Atmospheric Sciences, 73, 4221–4252, 2016.

Flynn, L. E., Homstein, J., and Hilsenrath, E.: The ozone mapping and profiler suite (OMPS). The next generation of US ozone monitoring instruments, in: Geoscience and Remote Sensing Symposium, 2004. IGARSS'04. Proceedings. 2004 IEEE International, vol. 1, IEEE, 2004.

Freudenthaler, V., Esselborn, M., Wiegner, M., Heese, B., Tesche, M., Ansmann, A., Müller, D., Althausen, D., Wirth, M., Fix, A., Ehret, G., Knippertz, P., Toledano, C., Gasteiger, J., Garhammer, M., and Seefeldner, M.: Depolarization ratio profiling at several wavelengths in pure Saharan dust during SAMUM 2006, Tellus B, 61, 165–179, 2009.

https://doi.org/10.5194/acp-2020-375
Preprint. Discussion started: 25 May 2020

Atmospheric Chemistry and Physics Discussions

Ginoux, P., Prospero, J. M., Gill, T. E., Hsu, N. C., and Zhao, M.: Global-scale attribution of anthropogenic and natural dust sources and their emission rates based on MODIS Deep Blue aerosol products, Reviews of Geophysics, 50, 2012.

Groß, S., Tesche, M., Freudenthaler, V., Toledano, C., Wiegner, M., Ansmann, A., Althausen, D., and Seefeldner, M.: Characterization of Saharan dust, marine aerosols and mixtures of biomass-burning aerosols and dust by means of multi-wavelength depolarization and Raman lidar measurements during SAMUM 2, Tellus B: Chemical and Physical Meteorology, 63, 706–724, 2011.

Groß, S., Freudenthaler, V., Schepanski, K., Toledano, C., Schäfler, A., Ansmann, A., and Weinzierl, B.: Optical properties of long-range transported Saharan dust over Barbados as measured by dual-wavelength depolarization Raman lidar measurements, Atmospheric Chemistry and Physics, pp. 11 067–11 080, 2015.

Haarig, M., Ansmann, A., Althausen, D., Klepel, A., Groß, S., Freudenthaler, V., Toledano, C., Mamouri, R.-E., Farrell, D. A., Prescod, D. A., et al.: Triple-wavelength depolarization-ratio profiling of Saharan dust over Barbados during SALTRACE in 2013 and 2014, Atmospheric Chemistry and Physics, 17, 10 767, 2017.

Hofer, J., Althausen, D., Abdullaev, S. F., Makhmudov, A. N., Nazarov, B. I., Schettler, G., Engelmann, R., Baars, H., Fomba, K. W., Müller, K., et al.: Long-term profiling of mineral dust and pollution aerosol with multiwavelength polarization Raman lidar at the Central Asian site of Dushanbe, Tajikistan: case studies, Atmospheric Chemistry and Physics, 17, 14 559, 2017.

Holben, B. N., Eck, T. F., Slutsker, I., Tanre, D., Buis, J., Setzer, A., Vermote, E., Reagan, J., Kaufman, Y., Nakajima, T., et al.: AERONET—A federated instrument network and data archive for aerosol characterization, Remote sensing of environment, 66, 1–16, 1998.

Hsu, N. C., Herman, J., Torres, O., Holben, B., Tanre, D., Eck, T., Smirnov, A., Chatenet, B., and Lavenu, F.: Comparisons of the TOMS aerosol index with Sun-photometer aerosol optical thickness: Results and applications, Journal of Geophysical Research: Atmospheres, 104, 6269–6279, 1999.

Hu, Q.: Advanced aerosol characterization using sun/sky photometer and multi-wavelength Mie-Raman lidar measurements, Ph.D. thesis, Lille 1, 2018.

Hu, Q., Goloub, P., Veselovskii, I., Bravo-Aranda, J.-A., Popovici, I. E., Podvin, T., Haeffelin, M., Lopatin, A., Dubovik, O., Pietras, C., et al.: Long-range-transported Canadian smoke plumes in the lower stratosphere over northern France, Atmospheric Chemistry and Physics, 19, 1173–1193, 2019.

Huang, J., Minnis, P., Chen, B., Huang, Z., Liu, Z., Zhao, Q., Yi, Y., and Ayers, J. K.: Long-range transport and vertical structure of Asian dust from CALIPSO and surface measurements during PACDEX, Journal of Geophysical Research: Atmospheres, 113, 2008.

Huang, K., Zhuang, G., Li, J., Wang, Q., Sun, Y., Lin, Y., and Fu, J. S.: Mixing of Asian dust with pollution aerosol and the transformation of aerosol components during the dust storm over China in spring 2007, Journal of Geophysical Research: Atmospheres, 115, 2010.

Huneeus, N., Schulz, M., Balkanski, Y., Griesfeller, J., Prospero, M., Kinne, S., Bauer, S., Boucher, O., Chin, M., Dentener, F., et al.: Global dust model intercomparison in AeroCom phase I, Atmospheric Chemistry and Physics, 11, 7781–7816, 2011.

Iwasaka, Y., Shi, G.-Y., Yamada, M., Matsuki, A., Trochkine, D., Kim, Y., Zhang, D., Nagatani, T., Shibata, T., Nagatani, M., et al.: Importance of dust particles in the free troposphere over the Taklamakan Desert: electron microscopic experiments of particles collected with a balloonborne particle impactor at Dunhuang, China, Journal of Geophysical Research: Atmospheres, 108, 2003.

Iwasaka, Y., Li, J., Shi, G.-Y., Kim, Y., Matsuki, A., Trochkine, D., Yamada, M., Zhang, D., Shen, Z., and Hong, C.: Mass transport of background Asian dust revealed by balloon-borne measurement: dust particles transported during calm periods by westerly from Taklamakan desert, in: Advanced environmental monitoring, pp. 121–135, Springer, 2008.

Jin, Y., Kai, K., Shibata, T., Zhang, K., and Zhou, H.: Validation of the dust layer structure over the Taklimakan Desert, China by the CALIOP space-borne lidar using ground-based lidar, Sola, 6, 121–124, 2010.

https://doi.org/10.5194/acp-2020-375
Preprint. Discussion started: 25 May 2020

Atmospheric Chemistry and Physics Discussions

Kai, K., Nagata, Y., Tsunematsu, N., Matsumura, T., Kim, H.-S., Matsumoto, T., Hu, S., Zhou, H., Abo, M., and Nagai, T.: The Structure of the Dust Layer over the Taklimakan Deser during the Dust Storm in April 2002 as Observed Using a Depolarization Lidar, Journal of the Meteorological Society of Japan. Ser. II, 86, 1–16, 2008.

Klett, J. D.: Lidar inversion with variable backscatter/extinction ratios, Applied Optics, 24, 1638–1643, 1985.

Kojima, T., Buseck, P. R., Iwasaka, Y., Matsuki, A., and Trochkine, D.: Sulfate-coated dust particles in the free troposphere over Japan, Atmospheric research, 82, 698–708, 2006.

Li, Z., Xu, H., Li, K., Li, D., Xie, Y., Li, L., Zhang, Y., Gu, X., Zhao, W., Tian, Q., et al.: Comprehensive study of optical, physical, chemical, and radiative properties of total columnar atmospheric aerosols over China: an overview of sun–sky radiometer observation network (SONET) measurements, Bulletin of the American Meteorological Society, 99, 739–755, 2018.

Littmann, T.: Dust storm frequency in Asia: climatic control and variability, International Journal of Climatology, 11, 393–412, 1991.

Liu, Z., Sugimoto, N., and Murayama, T.: Extinction-to-backscatter ratio of Asian dust observed with high-spectral-resolution lidar and Raman lidar, Applied Optics, 41, 2760–2767, 2002.

Moosmüller, H., Engelbrecht, J. P., Skiba, M., Frey, G., Chakrabarty, R. K., and Arnott, W. P.: Single scattering albedo of fine mineral dust aerosols controlled by iron concentration, Journal of Geophysical Research: Atmospheres, 117, 2012.

Murayama, T., Müller, D., Wada, K., Shimizu, A., Sekiguchi, M., and Tsukamoto, T.: Characterization of Asian dust and Siberian smoke with multi-wavelength Raman lidar over Tokyo, Japan in spring 2003, Geophysical Research Letters, 31, 2004.

Pan, X., Yan, P., Tang, J., Ma, J., Wang, Z., Gbaguidi, A., and Sun, Y.: Observational study of influence of aerosol hygroscopic growth on scattering coefficient over rural area near Beijing mega-city., Atmospheric Chemistry & Physics, 9, 2009.

Park, C. B., Sugimoto, N., Matsui, I., Shimizu, A., Tatarov, B., Kamei, A., Lee, C. H., Uno, I., Takemura, T., and Westphal, D. L.: Long-range transport of Saharan dust to east Asia observed with lidars, Sola, 1, 121–124, 2005.

Petrov, M. P. and S.Alitto, G.: Takla Makan Desert, https://www.britannica.com/place/Takla-Makan-Desert, 2019.

Qian, W., Quan, L., and Shi, S.: Variations of the dust storm in China and its climatic control, Journal of Climate, 15, 1216–1229, 2002.

Reed, K. A., Bacmeister, J. T., Huff, J. J. A., Wu, X., Bates, S. C., and Rosenbloom, N. A.: Exploring the Impact of Dust on North Atlantic Hurricanes in a High-Resolution Climate Model, Geophysical Research Letters, 46, 1105–1112, 2019.

Rolph, G., Stein, A., and Stunder, B.: Real-time environmental applications and display system: Ready, Environmental Modelling & Software, 95, 210–228, 2017.

Seftor, C., Jaross, G., Kowitt, M., Haken, M., Li, J., and Flynn, L.: Postlaunch performance of the Suomi National Polar-orbiting Partnership Ozone Mapping and Profiler Suite (OMPS) nadir sensors, Journal of Geophysical Research: Atmospheres, 119, 4413–4428, 2014.

Shi, Z., Zhang, D., Hayashi, M., Ogata, H., Ji, H., and Fujiie, W.: Influences of sulfate and nitrate on the hygroscopic behaviour of coarse dust particles, Atmospheric Environment, 42, 822–827, 2008.

Stein, A., Draxler, R. R., Rolph, G. D., Stunder, B. J., Cohen, M., and Ngan, F.: NOAA's HYSPLIT atmospheric transport and dispersion modeling system, Bulletin of the American Meteorological Society, 96, 2059–2077, 2015.

Sugimoto, N., Shimizu, A., Nishizawa, T., and Jin, Y.: Long-range transport of mineral dust observed with the Asian Dust and aerosol lidar observation Network (AD-Net), in: E3S Web of Conferences, vol. 99, EDP Sciences, 2019.

Sun, J. and Liu, T.: The age of the Taklimakan Desert, Science, 312, 1621–1621, 2006.

Tanaka, T. Y. and Chiba, M.: A numerical study of the contributions of dust source regions to the global dust budget, Global and Planetary Change, 52, 88–104, 2006.

https://doi.org/10.5194/acp-2020-375
Preprint. Discussion started: 25 May 2020

Atmospheric Chemistry and Physics Discussions

Tanaka, T. Y., Kurosaki, Y., Chiba, M., Matsumura, T., Nagai, T., Yamazaki, A., Uchiyama, A., Tsunematsu, N., and Kai, K.: Possible transcontinental dust transport from North Africa and the Middle East to East Asia, Atmospheric Environment, 39, 3901–3909, 2005.

Tesche, M., Ansmann, A., Mueller, D., Althausen, D., Mattis, I., Heese, B., Freudenthaler, V., Wiegner, M., Esselborn, M., Pisani, G., et al.: Vertical profiling of Saharan dust with Raman lidars and airborne HSRL in southern Morocco during SAMUM, Tellus B: Chemical and Physical Meteorology, 61, 144–164, 2009.

Textor, C., Schulz, M., Guibert, S., Kinne, S., Balkanski, Y., Bauer, S., Berntsen, T., Berglen, T., Boucher, O., Chin, M., et al.: Analysis and quantification of the diversities of aerosol life cycles within AeroCom, Atmospheric Chemistry and Physics, 6, 1777–1813, 2006.

Thompson, A. J., Skinner, C. B., Poulsen, C. J., and Zhu, J.: Modulation of mid-Holocene African rainfall by dust aerosol direct and indirect effects, Geophysical Research Letters, 46, 3917–3926, 2019.

Uno, I., Eguchi, K., Yumimoto, K., Takemura, T., Shimizu, A., Uematsu, M., Liu, Z., Wang, Z., Hara, Y., and Sugimoto, N.: Asian dust transported one full circuit around the globe, Nature Geoscience, 2, 557–560, 2009.

VanCuren, R. A. and Cahill, T. A.: Asian aerosols in North America: Frequency and concentration of fine dust, Journal of Geophysical Research: Atmospheres, 107, AAC–19, 2002.

Veselovskii, I., Goloub, P., Podvin, T., Bovchaliuk, V., Derimian, Y., Augustin, P., Fourmentin, M., Tanre, D., Korenskiy, M., Whiteman, D., et al.: Retrieval of optical and physical properties of African dust from multiwavelength Raman lidar measurements during the SHADOW campaign in Senegal, Atmos. Chem. Phys, 16, 7013–7028, 2016.

Veselovskii, I., Hu, Q., Goloub, P., Podvin, T., Korenskiy, M., Derimian, Y., Legrand, M., and Castellanos, P.: Variability of Lidar-Derived Particle Properties Over West Africa Due to Changes in Absorption: Towards an Understanding, Atmospheric Chemistry and Physics Discussions, 2020, 1–37, https://doi.org/10.5194/acp-2020-98, https://www.atmos-chem-phys-discuss.net/acp-2020-98/, 2020.

Yu, Y., Kalashnikova, O. V., Garay, M. J., and Notaro, M.: Climatology of Asian dust activation and transport potential based on MISR satellite observations and trajectory analysis, Atmospheric Chemistry and Physics, 19, 363–378, 2019.

Yumimoto, K., Eguchi, K., Uno, I., Takemura, T., Liu, Z., Shimizu, A., and Sugimoto, N.: An elevated large-scale dust veil from the Taklimakan Desert: Intercontinental transport and three-dimensional structure as captured by CALIPSO and regional and global models, Atmospheric Chemistry and Physics, 9, 8545–8558, 2009.

https://doi.org/10.5194/acp-2020-375
Preprint. Discussion started: 25 May 2020

Atmospheric Chemistry and Physics Discussions

Table 1. Daily averaged AOD at 500 nm and Ångström exponent (between 440 and 870 nm) measured by the sun/sky photometer in daytime. The values on the right side of '±' represent the standard deviation of the values on the left side.

	AOD_{500}	$AE_{440-870}$
Case 1, 09 April	1.48±0.10	0.04±0.02
Case 2, 24 April	3.63±1.28	-0.01±0.03
Case 3, 15 April	0.63±0.03	0.10±0.02
Case 4, 03 April	0.49±0.16	0.11±0.03

Table 2. A summary of optical properties derived from lidar observations in the case studies. The values before the '±' symbol represent the mean in the range of the layer height. The values after the '±' symbol represent the statistical error of the values before the symbol.

	Case 1: dust haze 15:00–16:00 09 April	**Case 2: dust storm** 15:00–16:00 24 April	**Case 3: polluted dust** 15:00–16:00 15 April		**Case 4: polluted dust** 15:00–16:00 03 April	
Layer height [m]	800–3800	800–2000	1000–2200	2400–2800	1000–1500	1500–3000
$PLDR_{355}$	0.32±0.05	0.32±0.05	0.32±0.05	0.23±0.03	0.30–0.32±0.05	0.21±0.03–0.29±0.04
$PLDR_{532}$	0.36±0.05	0.36±0.05	0.34±0.05	0.26±0.03	0.35±0.05	0.28±0.04–0.34±0.05
(V)$PLDR_{1064}$	0.31±0.04[a]	–	0.31±0.04	0.24±0.03	0.32±0.05	0.28±0.04–0.33±0.05
LR_{355} [sr]	56±8	55[b]	51±8	42±6	51±8	43±6–57±8
LR_{532} [sr]	46±7	45[b]	45±7	40±6	45±7	38±6–49±8
$EAE_{355-532}$	-0.01±0.30	0.01±0.3	0.02±0.30	0.10±0.30	0.02±0.30	0.14±0.30–0.30±0.30
$BAE_{355-532}$	-0.51±0.30	–	-0.29±0.30	-0.06±0.30	-0.29±0.30	-0.13±0.30–0.20±0.30
RH [%]	20±4–60±12	10±2–20±4	30±6–60±12	80±16	20±4–60±12	45±9–70±14
WVMR [g/kg]	2.2±0.5	–	3.5±7	4.0±0.8	2.7±0.6	2.7±0.6

[a] $PLDR_{1064}$ is not available in this case, but $VLDR_{1064}$ is. We assume $VLDR_{1064} \approx PLDR_{1064}$ considering aerosol scattering is much stronger than molecular scattering. [b] 55 and 45 sr are assumed lidar ratios based on the results in Case 1.

https://doi.org/10.5194/acp-2020-375
Preprint. Discussion started: 25 May 2020

Atmospheric Chemistry and Physics Discussions

Table 3. A review of dust lidar ratios and particle linear depolarization ratios in literatures. The values of lidar ratios and PLDRs, as well as their errors are based on the results in the references. Error estimates are not provided if their are not available in the original publication.

Dust source	Observation site	PLDRs			LRs		Reference
		355	532	1064	355	532	
Saharan dust	Ouarzazate[1a]	–	0.30	–	–	38–50	Esselborn et al. (2009)
	Ouarzazate[1b]	–	–	–	53–55	53–55	Tesche et al. (2009)
	Cape Verde	0.24–0.27	0.29–0.31	–	48–70	48–70	Groß et al. (2011)
	M'bour[2a]	–	0.34±0.05	–	68±10	50±8	Veselovskii et al. (2016)
	M'bour[2b]	–	0.32±0.05	–	55–60±9	55–60±8	Veselovskii et al. (2020)
	Leipzig	–	0.15-0.25		50–90	40–80	Ansmann et al. (2003)
	Barbados	0.26±0.03	0.27±0.01	–	53±5	56±7	Groß et al. (2015)
	Barbados	0.25±0.03	0.28±0.02	0.23±0.02	40–60	40–60	Haarig et al. (2017)
Asian dust	Aksu	–	–	–	–	42±3	Jin et al. (2010)
	Japan	–	0.20	–	49	43	Murayama et al. (2004)
	Kazan	0.23±0.02	–	–	43±14	–	Dieudonné et al. (2015)
	Omsk	0.17±0.02	–	–	50±13	–	
	Dushanbe[3a]	0.23±0.01	0.35±0.01	–	47±2	43±3	Hofer et al. (2017)
	Dushanbe[3b]	0.29±0.01	0.35±0.01	–	40±1	39±1	
	Kashi	0.28±0.04 – 0.32±0.05	0.35±0.05	0.31±0.05	51±8 – 56±8	45±7	This study
American dust	Chihuahuan	0.24±0.05	0.37±0.02	0.38±0.01	–	–	Burton et al. (2015)
	Pico de Orizaba	–	0.33±0.02	0.40±0.01	–	–	Burton et al. (2015)

[1a]HSRL measurements; [1b]Raman lidar measurement; [2a] 29 March 2015 in the dry season; [2b]23–24 April 2015 in the transition period [3a]Extreme dust case on 8 August 2015, [3b]Most extreme dust case on 14 July 2016

https://doi.org/10.5194/acp-2020-375
Preprint. Discussion started: 25 May 2020

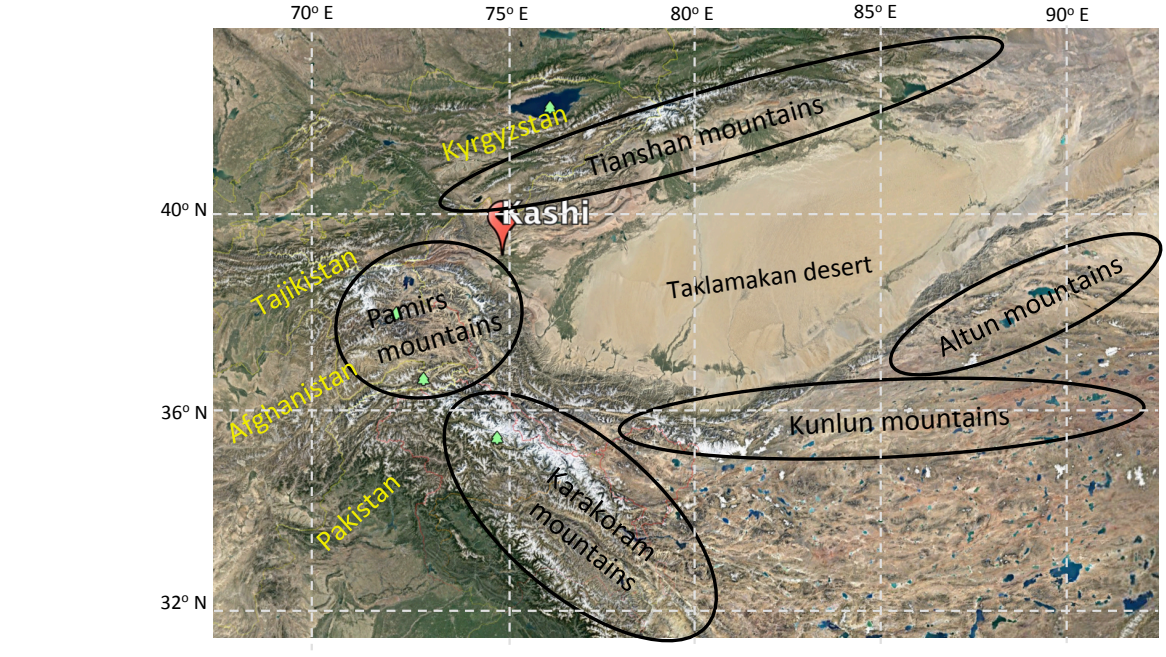

Figure 1. The location of the observation site in Kashi. The black ellipses indicate the mountain ranges surrounding the Taklamakan desert, including the Tianshan mountains, the Pamir mountains, the Karakoram mountains, the Kunlun and Altun mountains. @ Google Maps 2020.

https://doi.org/10.5194/acp-2020-375
Preprint. Discussion started: 25 May 2020

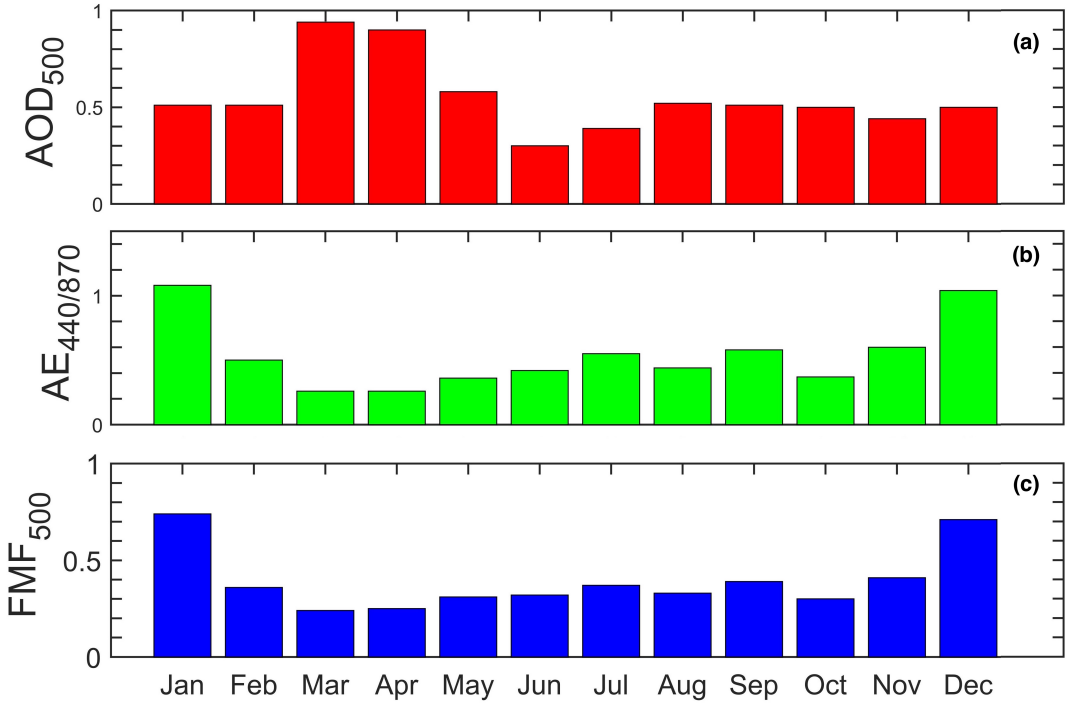

Figure 2. Monthly means of (a) the AOD at 500 nm, (b) Angström exponent (440–870) and (c) FMF at 500 nm from 2013 to 2017. The data are obtained from the SONET network.

https://doi.org/10.5194/acp-2020-375
Preprint. Discussion started: 25 May 2020

Atmospheric Chemistry and Physics Discussions

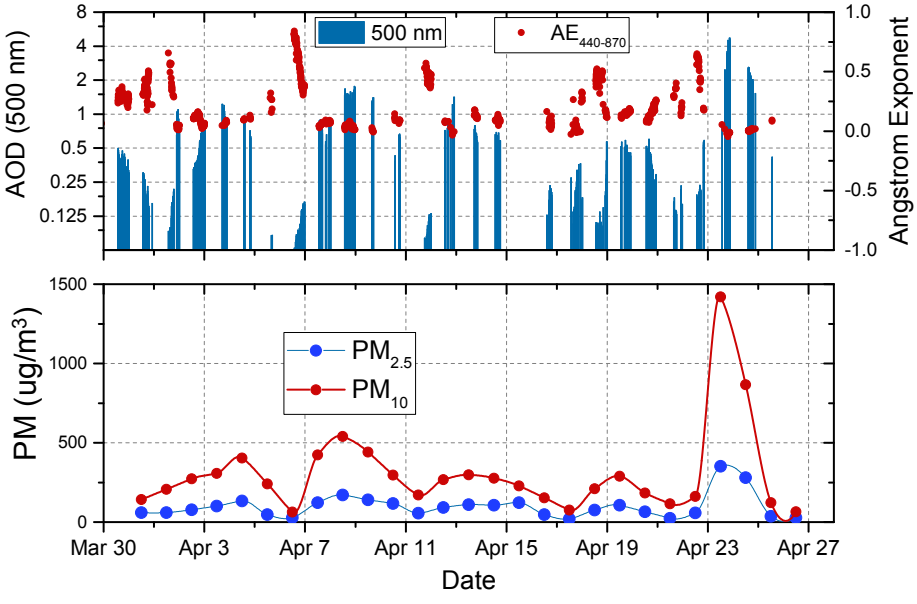

Figure 3. The AOD, Angström exponent and daily particulate matter (in $\mu g\, m^{-3}$) in April 2019. The AOD and AE are measured by the sun/sky photometer deployed in Kashi site, and the data are stored in the SONET network. The particulate matter data come from the meteorological station, 5 km to the observation site.

https://doi.org/10.5194/acp-2020-375
Preprint. Discussion started: 25 May 2020

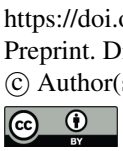

Atmospheric Chemistry and Physics Discussions

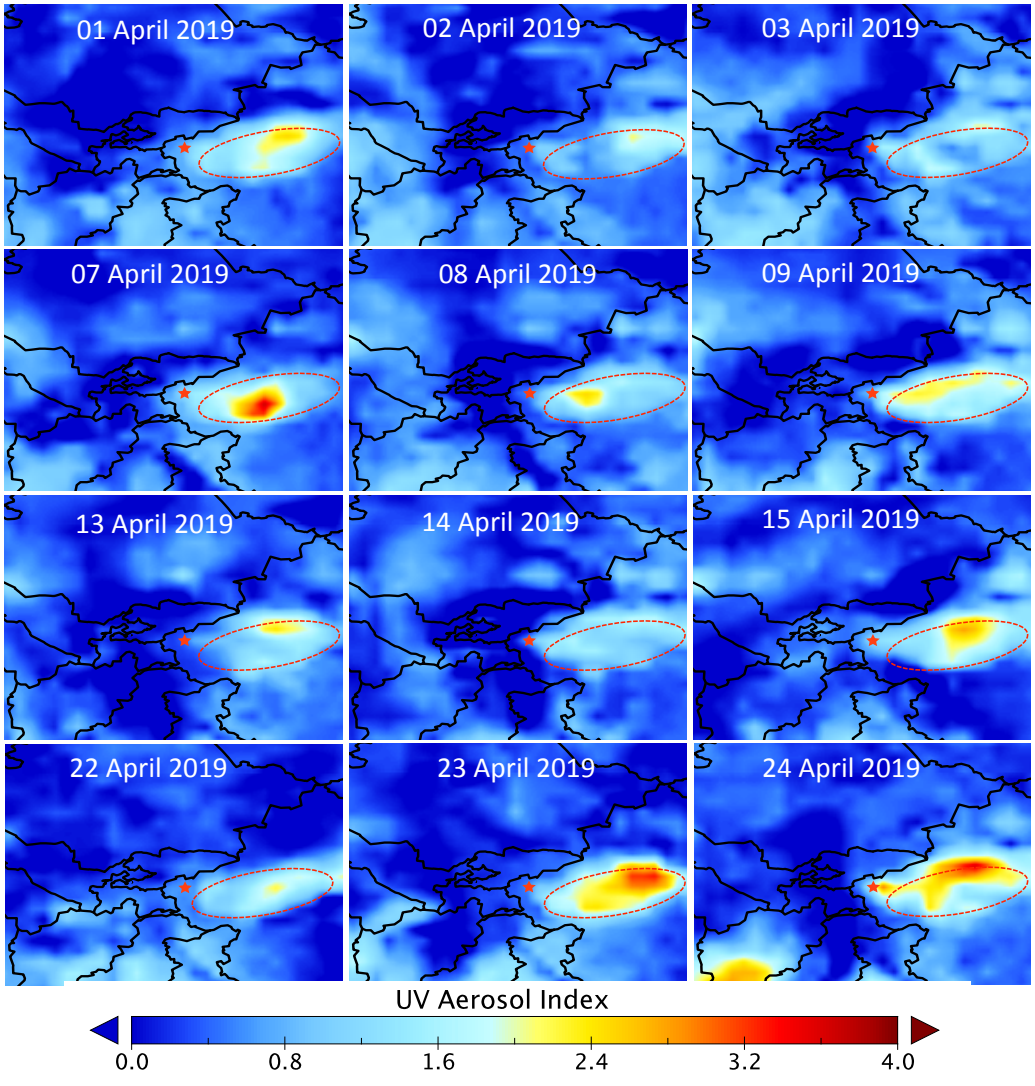

Figure 4. The UVAI derived from OMPS instrument onboard the Suomi-NPP satellite. The red star represents the location of the observation site. The dashed red ellipse represents the location of the Taklamakan desert.

https://doi.org/10.5194/acp-2020-375
Preprint. Discussion started: 25 May 2020

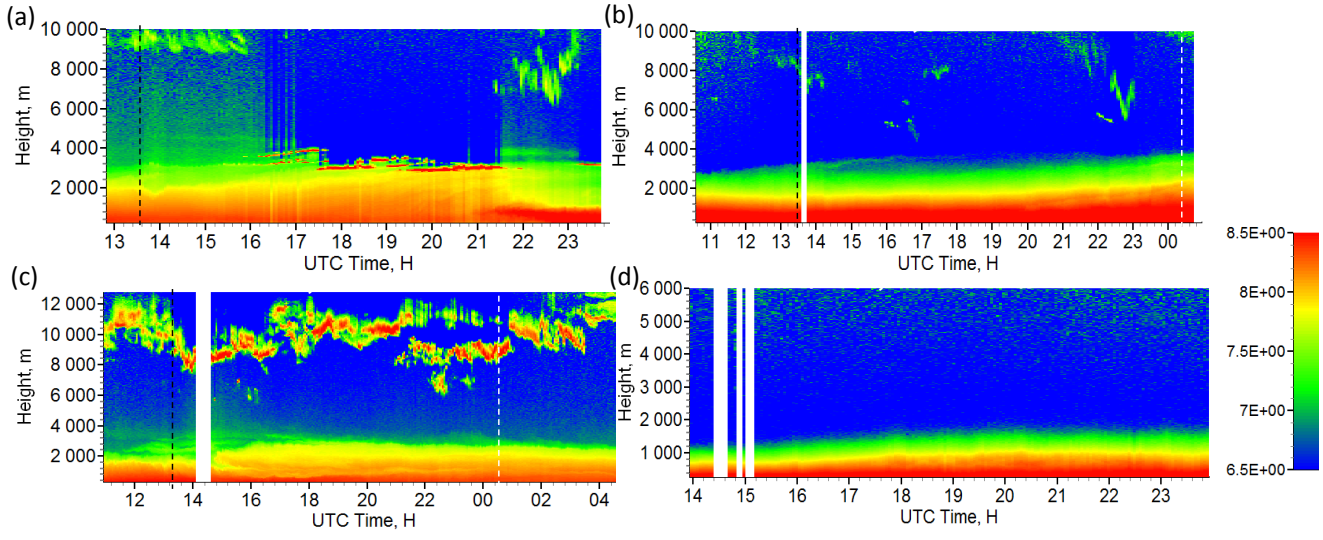

Figure 5. The quicklook of the range-corrected lidar siganl at 532 nm in the four cases: (a) Case 4: 03 April 2019, (b) Case 1: 09 April 2019, (c) Case 3: 15 April 2019and (d) Case 2: 24 April 2019. The dashed black lines represent the sunset time and dashed white lines represent the sunrise time.

https://doi.org/10.5194/acp-2020-375
Preprint. Discussion started: 25 May 2020

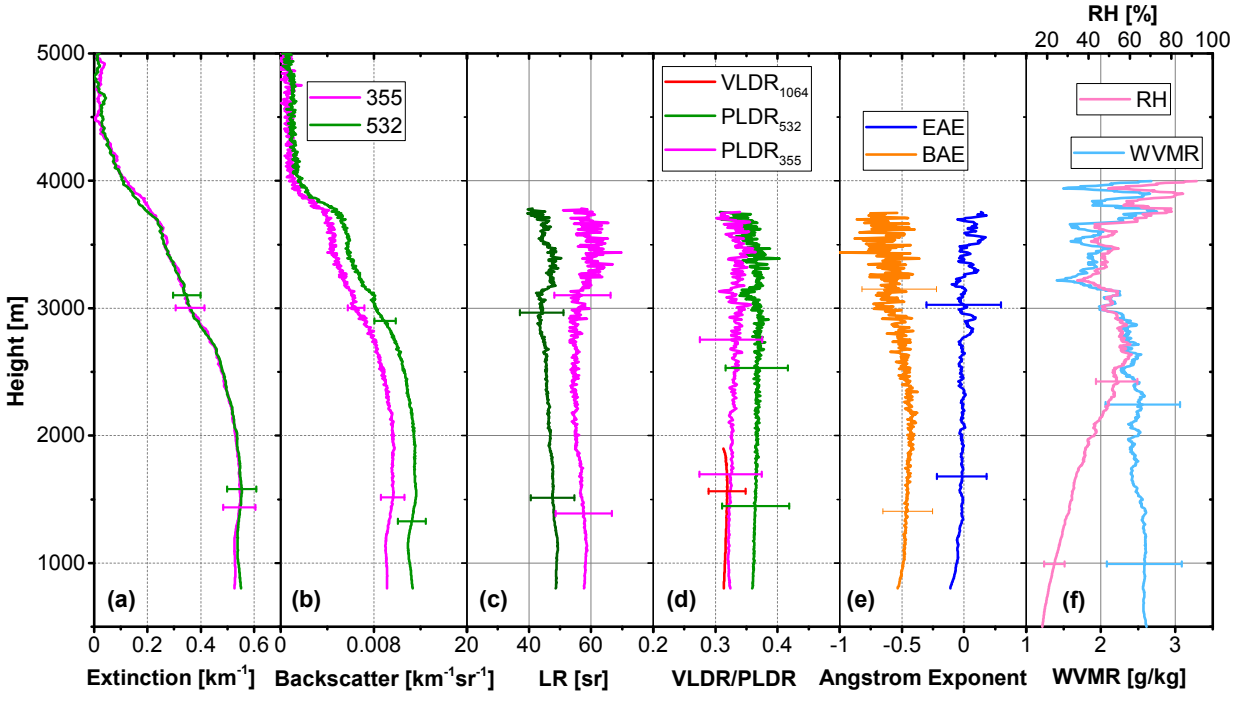

Figure 6. Case 1: Lidar derived parameters at 17:00–22:00 UTC, 09 April 2019. (a) Extinction coefficient, (b) backscattering coefficient, (c) lidar ratio, (d) PLDR/VLDR, (e) Angström expoent and (f) WVMR and relative humidity.

https://doi.org/10.5194/acp-2020-375
Preprint. Discussion started: 25 May 2020

Atmospheric Chemistry and Physics Discussions

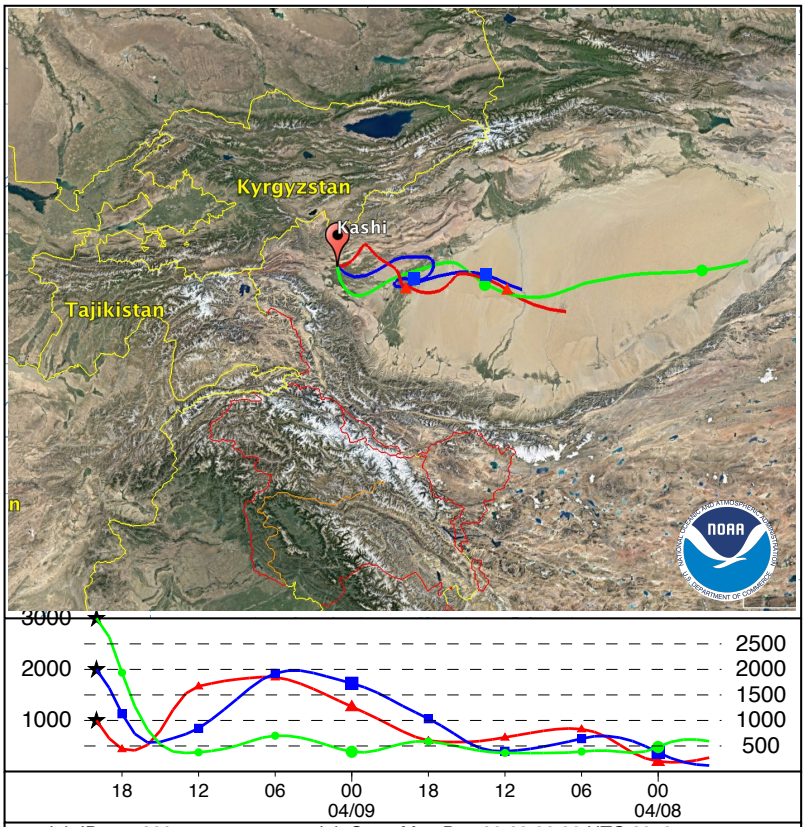

Figure 7. Case 1: The 48-hour back trajectories ending at 19:00 UTC, 09 April 2019 for air mass at 1000, 2000 and 3000 m. @ Google Maps 2020.

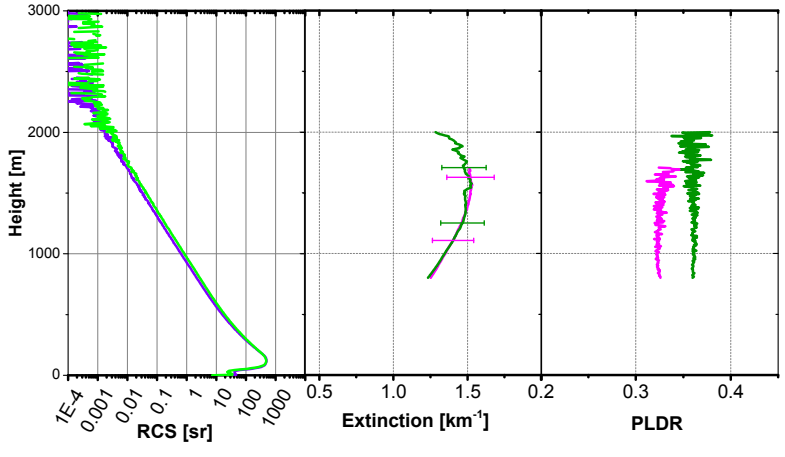

Figure 8. Case 2: Lidar derived parameters at 15:00–24:00 UTC, 24 April 2019. (a) The Raman lidar signals at 530 and 387 nm. (b) The extinction coefficients at 355 and 532 nm. (c) The PLDRs at 355 and 532 nm.

https://doi.org/10.5194/acp-2020-375
Preprint. Discussion started: 25 May 2020

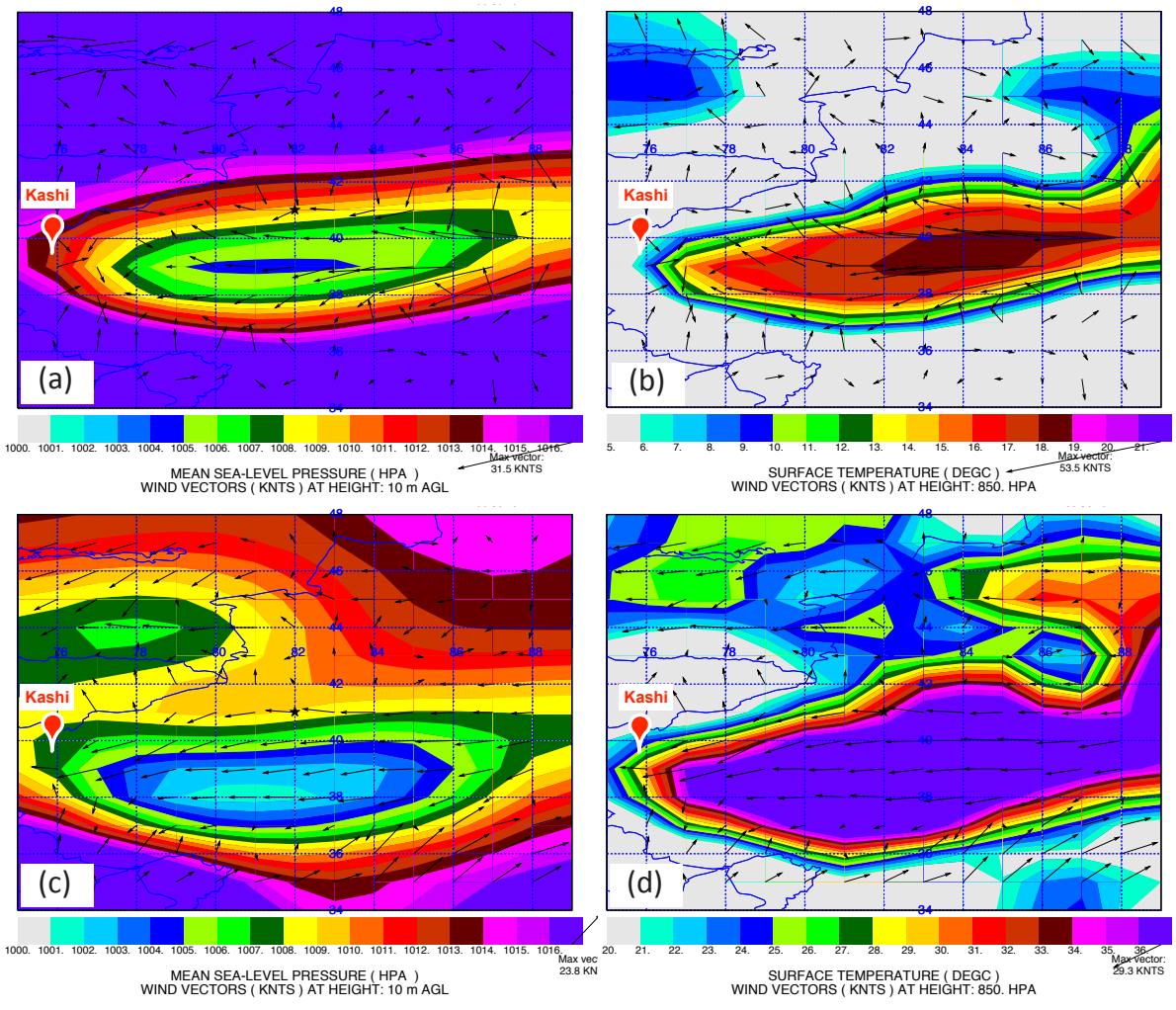

Figure 9. Case 2: The synoptic condition at 06:00 UTC, 24 April 2019. The data are obtained from the 1-degree GDAS archived meteorological data. (a) The mean sea level pressure at the surface overlaid with wind vector at 10 m above the ground level. (b) The temperature at 2 m vertical level overlaid with wind vector at 850 hPa vertical level.

https://doi.org/10.5194/acp-2020-375
Preprint. Discussion started: 25 May 2020

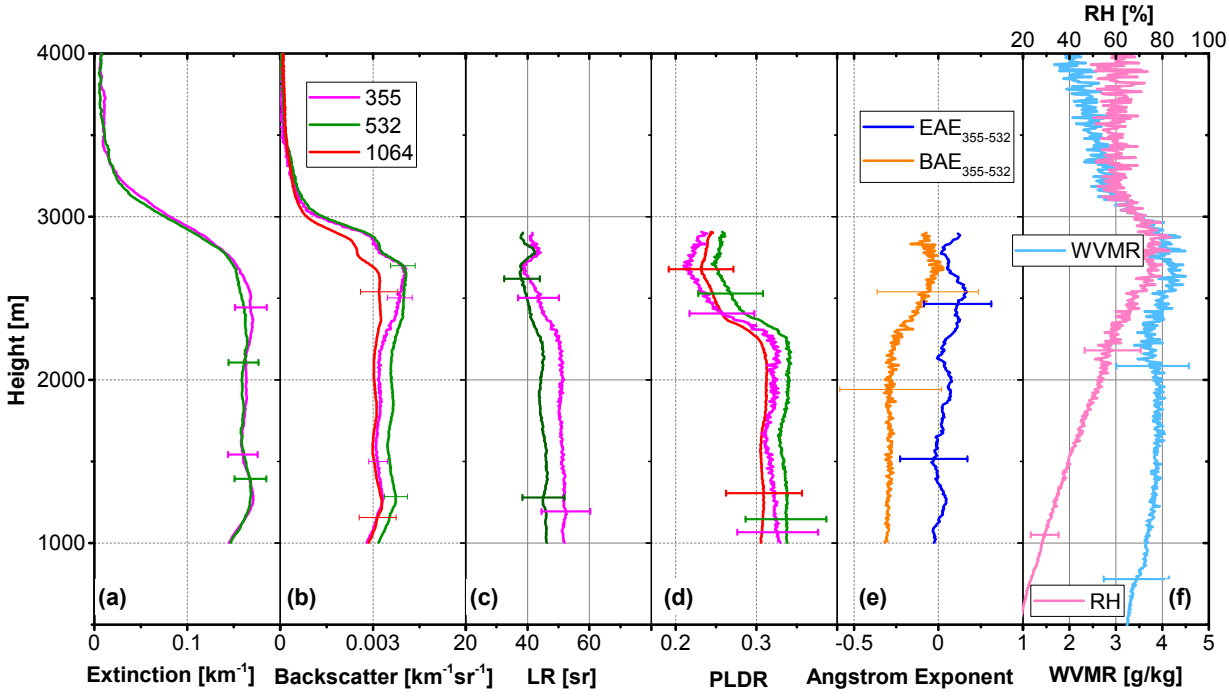

Figure 10. Case 3: Lidar derived parameters at 18:00–20:00 UTC, 15 April 2019. (a) Extinction coefficient, (b) backscattering coefficient, (c) lidar ratio, (d) PLDR, (e) Ångström exponent and (f) WVMR and relative humidity.

https://doi.org/10.5194/acp-2020-375
Preprint. Discussion started: 25 May 2020

Atmospheric Chemistry and Physics Discussions

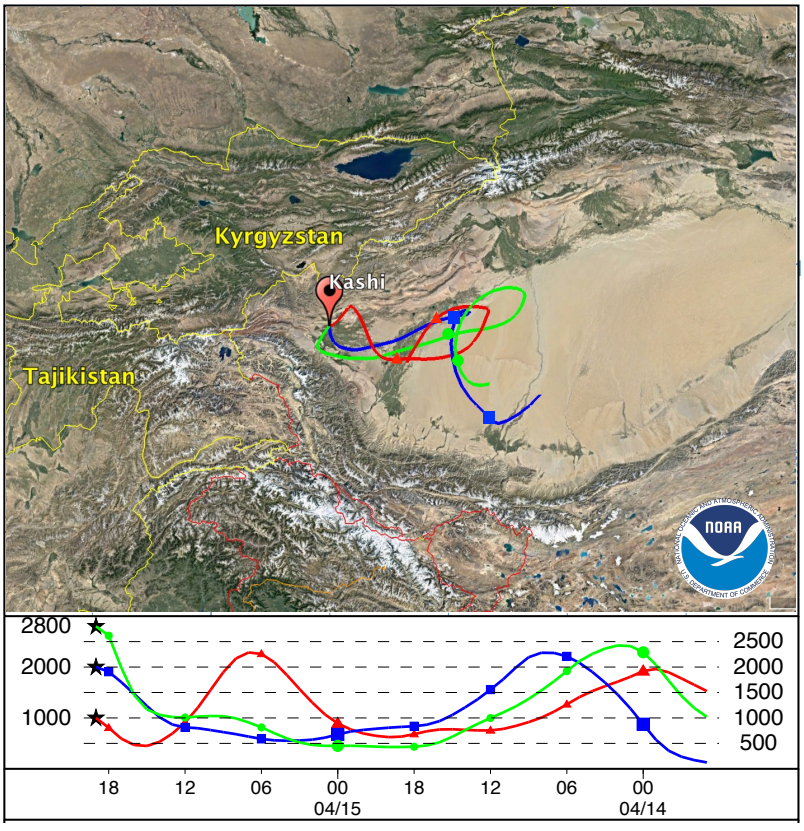

Figure 11. Case 3: The 48-hour back trajectories ending at 19:00 UTC, 15 April 2019 for air mass at 1000, 2000 and 2800 m. @ Google Maps 2020.

https://doi.org/10.5194/acp-2020-375
Preprint. Discussion started: 25 May 2020

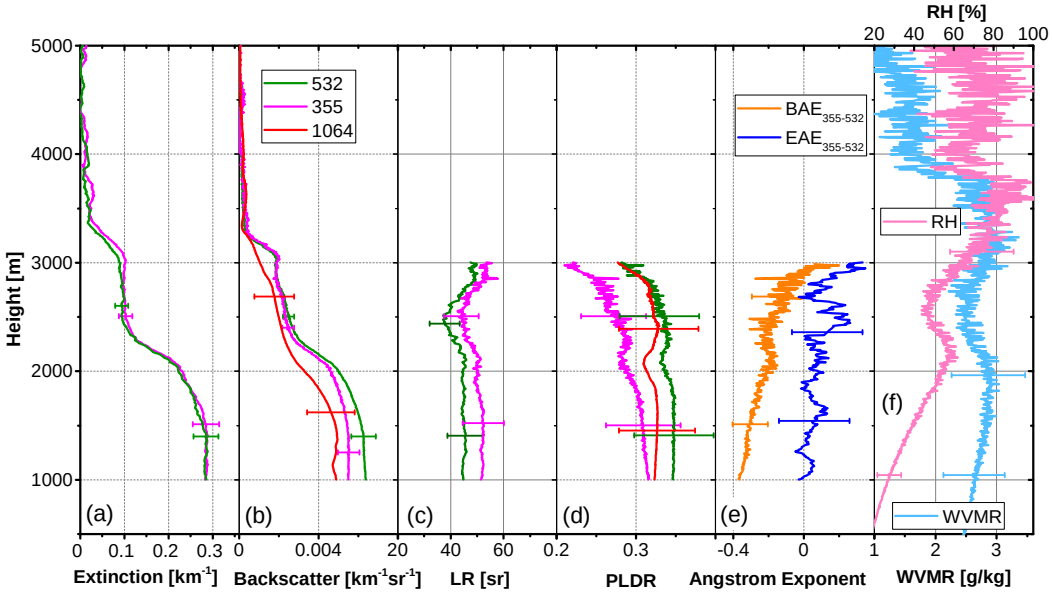

Figure 12. Case 4: Lidar derived parameters at 14:00–16:00 UTC, 03 April 2019. (a) Extinction coefficient, (b) backscattering coefficient, (c) lidar ratio, (d) PLDR, (e) Ångström exponent and (f) WVMR and relative humidity.

https://doi.org/10.5194/acp-2020-375
Preprint. Discussion started: 25 May 2020

Atmospheric Chemistry and Physics Discussions

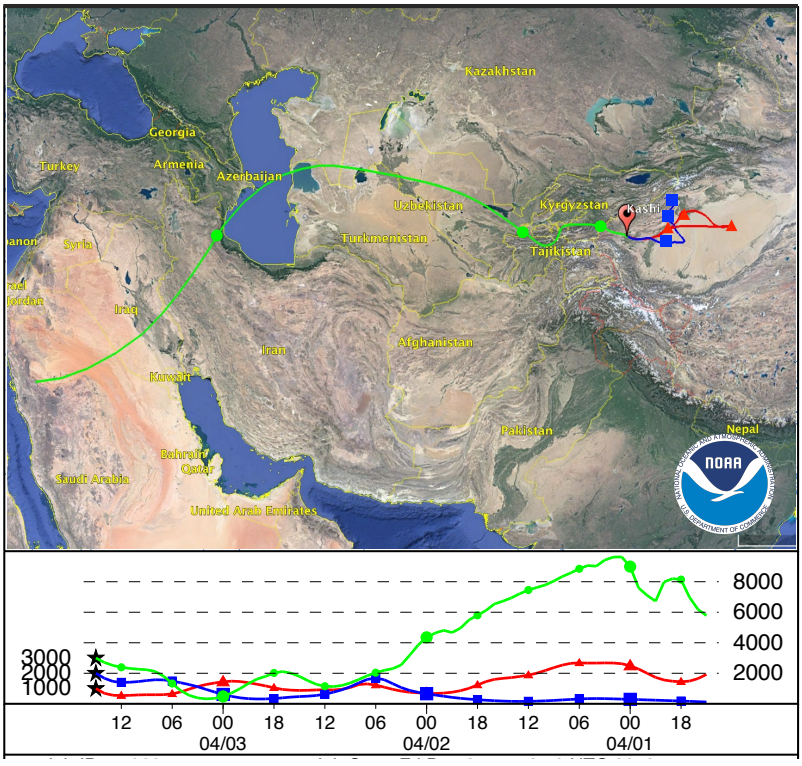

Figure 13. Case 4: The 72-hour back trajectories ending at 15:00 UTC, 03 April 2019 for air mass at 1000, 2000 and 3000 m. @ Google Maps 2020.

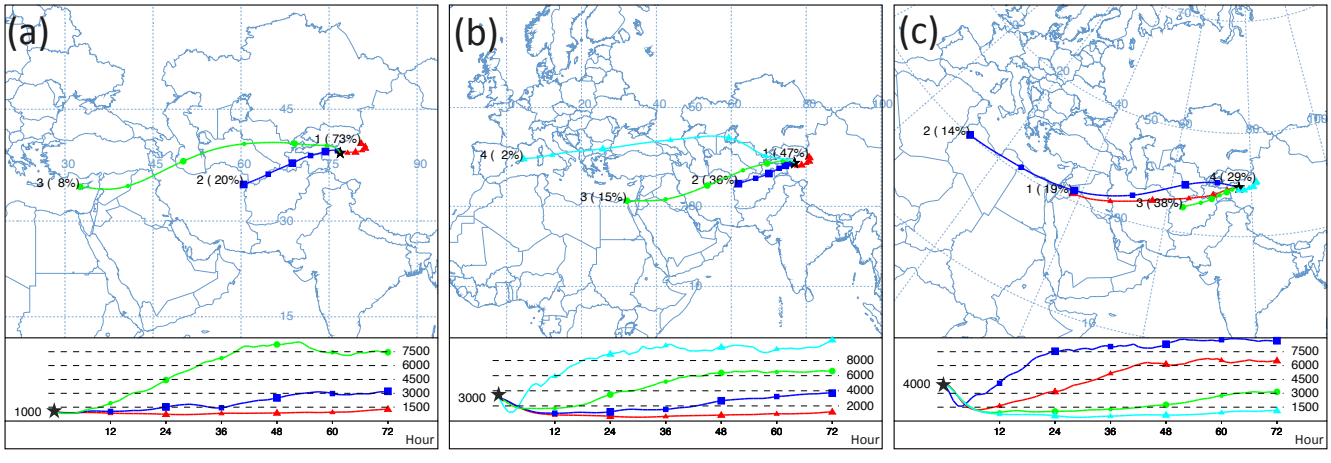

Figure 14. The clustering of air mass in April 2019. The clustering is performed using HYSPLIT and based on back trajectories with a 2-hour time resolution and 72-hour duration. (a) 1000 m, (b) 3000 m, (c) 4000 m.